ARTICLE

Free-Standing Bimetallic Nanorings and Nanoring Arrays Made by On-Wire Lithography

Cipto Liusman,[†,‡] Shuzhou Li,[†] Xiaodong Chen,[‡,§] Wei Wei,[†] Hua Zhang,[‡,§,*] George C. Schatz,[†,*] Freddy Boey,[‡,§,*] and Chad A. Mirkin[†,*]

[†]Department of Chemistry and International Institute for Nanotechnology, Northwestern University, 2145 Sheridan Road, Evanston, Illinois 60208-3113, United States, [‡]School of Materials Science and Engineering, Nanyang Technological University, 50 Nanyang Avenue, Singapore 639798, Singapore, and [§]Center for Biomimetic Sensor Science, Nanyang Technological University, 50 Nanyang Drive, Singapore 637553, Singapore

ABSTRACT This paper describes a new strategy for synthesizing free-standing bimetallic nanorings and nanoring arrays based upon on-wire lithography and a galvanic replacement reaction. The strategy allows one to tune the diameter, length, and therefore aspect ratio of the nanorings. In addition, it can be used to produce arrays of nanorings in high yield with control over number and spacing. Spectroscopic studies and discrete dipole approximation calculations show that nanoring dimers exhibit greater surface enhanced Raman scattering than the analogous nanodisk dimers.

KEYWORDS: nanorings · nanoring arrays · on-wire lithography · galvanic replacement reaction · surface-enhanced Raman scattering

The plasmonic properties of noble metal nanostructures have been utilized in a variety of applications, including subwavelength optics,[1] biological and chemical sensing,[2] spectroscopic enhancing,[3] and solar cells.[4] Indeed, over the past few decades, there have been extensive efforts to synthesize and control the size and shape of metallic nanostructures since such parameters enable the tuning of plasmon resonance wavelengths. Many nanostructures, including triangular nanoprisms,[5] bipyramids,[6] nanorods,[7] nanoshells,[8] and nanocubes,[9] have been synthesized and studied with respect to their plasmonic activity. Shell structures are particularly interesting because they allow independent tuning of plasmons associated with inner and outer surfaces as well as variation in the coupling of these resonances. Specifically, the anisotropic structure of rings with variable longitudinal and transverse axes provides significant tailorability for adjusting plasmon resonance wavelengths and intensities. Furthermore, nanorings have a large surface-to-volume ratio, which reduces radiation damping[10] and leads to strong signals in surface-enhanced Raman scattering (SERS). Attempts to fabricate metallic nanorings have involved nanosphere- or colloidal lithography,[11−15] electron beam lithography,[16] anodized aluminum oxide (AAO) template-assisted methods,[17] and molecular template methods.[18,19] Nanosphere lithography, in particular, provides the ability to control the diameter and wall thickness of the nanorings. However, none of these methods independently allows one to produce free-standing and dispersible ring or ring-array structures in high yield with control over ring diameter, length, and therefore aspect ratio. Moreover, it is exceedingly difficult to fabricate nanoring arrays with the longitudinal ring axes of the rings parallel to the substrate. Such capabilities afford researchers with ability to create spectroscopically encoded structures that can be used as labels for biological and chemical detection and other forms of taggants.[20,21]

On-wire lithography (OWL) is an emerging technique that has been used to create disk architectures, gapped nanowires, and single or multicomponent nanowire structures with sub-10 nm resolution in high yield at moderately high throughput.[22] With OWL, one can fabricate many types of metal and polymer nanostructures with control over feature dimensions from 2 nm to many micrometers. OWL has been used to prepare molecular transport junctions,[23−25] electrical nanotraps,[26] plasmonic disk arrays,[20,21] catalytic nanorotors,[27] and novel energy conversion materials.[28] In other work, galvanic replacement reactions (GRRs) have been utilized for making hollow nanostructures, such as nanotriangles,[29] cylindrical Au/Ag alloy

*Address correspondence to chadnano@northwestern.edu, schatz@chem.northwestern.edu, mycboey@ntu.edu.sg, hzhang@ntu.edu.sg.

Received for review September 22, 2010 and accepted November 2, 2010.

Published online November 11, 2010. 10.1021/nn102495f

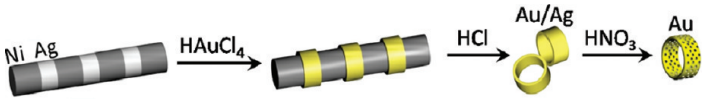

Scheme 1. Scheme illustrating the OWL technique used to fabricate nanorings. Striped Ag−Ni nanorods (prepared by electrochemical deposition) are used as templates for a galvanic replacement reaction (GRR) followed by selective wet chemical etching of Ni and Ag.

nanostructures,[30] and nanocages,[9] from triangular prisms, cylinders, and cubes, respectively.

In this paper, we demonstrate how Ag disk architectures, prepared by OWL or striped wire synthesis,[31] can be chemically converted into Au/Ag nanoring and nanoring array structures using a GRR. This capability allows one to study a novel class of ring array nanostructures and systematically tailor their plasmonic properties. Importantly, our study shows that Au/Ag alloy nanoring structures have localized surface plasmon resonances (LSPR) that can span the visible and near-infrared spectra. In addition, we combine the electrodynamic modeling and SERS experiments to study the plasmonic behavior of these novel nanostructures.

RESULTS AND DISCUSSION

In a typical experiment, electrochemical template-based methods were used to prepare striped Ag−Ni nanorod structures[28] (Scheme 1). The segment lengths were controlled by the total charge passed during electrochemical deposition (Supporting Information, Figure S1). These structures were treated with $HAuCl_4$, which causes a GRR with only the Ag segments and converts them into alloy ring structures (eq 1). Since Ni does not react with $HAuCl_4$, it serves as an excellent capping and separation material for the Ag segments (*i.e.*, the ends of the Ag segments are directly exposed to the $HAuCl_4$).

$$3Ag(s) + AuCl_4^-(aq) \rightarrow 3Ag^+(aq) + Au(s) + 4Cl^-(aq) \quad (1)$$

Finally, dispersible "solid" nanorings were obtained by etching the Ni segments in 37% HCl. Further etching of these solid structures in 70% HNO_3 results in dissolution of the Ag and formation of porous nanorings (Scheme 1).

The Ag−Ni nanorods have a diameter of 360 ± 26 nm with Ag and Ni segment lengths of 193 ± 14 nm and 310 ± 34 nm, respectively, as evidenced by SEM (Figure 1a). After the GRR, the nanorings appear as raised features surrounding what used to be the Ag segments (Figure 1b). The average length of the released nanorings is 209 ± 34 nm (Figure 1c) which is comparable to the length of the original pure Ag segments. The average wall thickness of the nanorings is 33 ± 9 nm. The corresponding EDX spectrum (Supporting Information, Figure S2) confirms that the nanorings are alloys of Au and Ag (1:1.7). Au content can be increased by increasing the amount of $HAuCl_4$, but pure solid Au ring structures cannot be obtained because at large excesses of $HAuCl_4$ to Ag, porous ring structures are obtained. Indeed, one can show that other Ag etchants, such as 70% HNO_3, also will dissolve the Ag in the bimetallic ring structures to generate porous structures (Figure 1d).[32] The resulting structures have higher Au/Ag ratios (~10:1) but never reach purity with respect to Au. Apparently, some of the Ag atoms are physically encapsulated in Au preventing the completion of the etching process.

We investigated the plasmonic behavior of solid and porous nanorings by SERS. Both types of nanorings were functionalized with methylene blue (MB) and characterized by Raman microscopy (WiTec Alpha 300). The laser used was a 632.8 nm He−Ne laser (Coherent Inc., Santa Clara, CA) with a power density of ~10^4 W/cm^2. 3D Raman microscopy images were obtained by integrating the spectra intensity from 1600−1660 cm^{-1}; there is a strong ring stretching (υ(CC)) mode for MB at 1628 cm^{-1}.[33] The Raman microscopy images of the porous nanoring structures exhibit SERS signals approximately six times larger than the solid ring structures, which can be attributed in part to the larger surface area of the porous structures (Figure 2a,b). New hot spots created by the nanopores might also be contributors to this increased response. The highest enhancement appears to be in the middle of the nanorings, even though the molecules are localized on the interior and exterior surface of nanorings. This observation is a consequence of the spatial resolution limit of the microscope. The Raman spectra of MB taken from both porous and solid nanorings also show that porous nanorings have larger signals than solid nanorings by up to about 6 times (Figure 2c). In this geometric configuration, only the transverse modes of the nanostructures were excited by the laser.

To further investigate enhancement, electrodynamic modeling was done using the discrete dipole approximation (DDA).[34] Previous work has demonstrated that the extinction spectra and SERS enhancement factors calculated with this method are generally in excellent agreement with experiment.[35,36] All DDA calculations were performed using DDSCAT7.0.[37] The gold and silver dielectric constants are from Johnson and Christy[38] and Palik,[39] respectively. The alloy dielectric constants are determined from a volume average of their components. The grid spacing is 4 nm in all calculations. The electromagnetic enhancement factor (EF) in SERS is taken to be g^4 ($g = |E|/|E_0|$), where E and E_0 are the local and incident fields, respectively, at the particle surfaces. To model Raman measurements for the nanostructures, the enhancement factor (EF) is calcu-

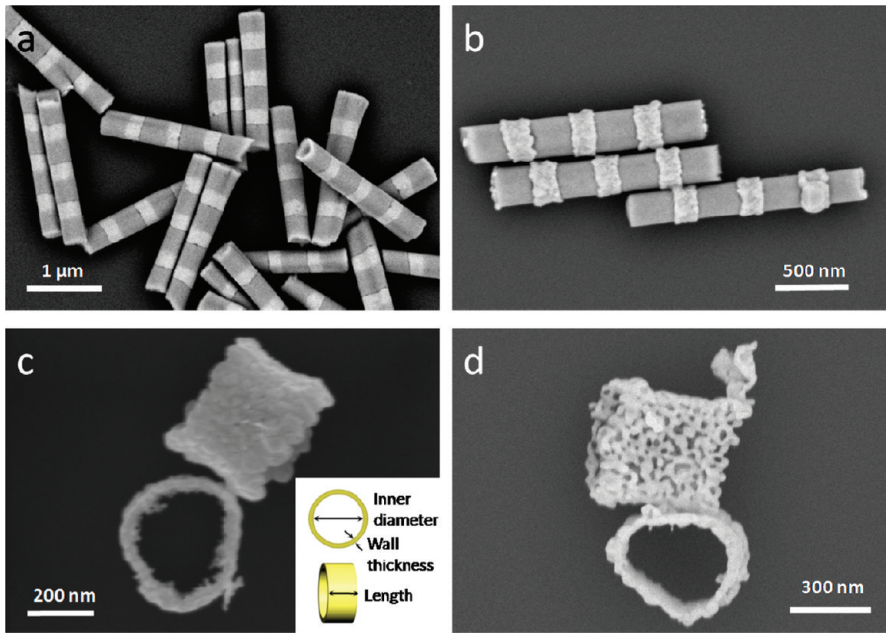

Figure 1. SEM images of (a) striped Ag−Ni nanorods prepared by electrochemical deposition, (b) striped nanorods after GRR, (c) bimetallic solid nanorings, and (d) porous nanorings.

lated using EF = $\int g^4 dS / \int dS$, which averages the electromagnetic enhancement over the available surface area.

The LSPR positions of the nanorings can be tuned by varying their diameter, thickness, and length. In our experiments, they were tuned by the length of the nanorings, which can be easily controlled in the electrochemical deposition process. To excite the longitudinal mode (Figure 2d), the nanorings are placed on a substrate with the longitudinal axis parallel to the substrate while the laser is radiated perpendicularly to the surface, with polarization along the longitudinal axes of the nanorings. Supporting Information, Figure S4 shows an example of length tunability of the nanorings (85 ± 24 nm in length with wall thickness of 37 ± 13 nm). However, since nanorings with these aspect ratios (360 nm inner diameter and <200 nm in length) tend to lie down on the substrate, only the transverse mode is excited.

With a slight modification of our synthesis method, it is possible to fabricate nanoring arrays with well-defined positioning of the nanorings on a substrate (*i.e.*, the longitudinal axes are parallel to substrate). After the GRR with the nanorods, they were coated with 50 nm of silica on one side by plasma-enhanced chemical vapor deposition (PECVD). Nickel segments were then removed by wet chemical etching to give nanoring arrays (Figure 3a). These nanoring arrays also make it possible to fabricate dimers (referring to just two particles), which are known to increase the Raman signal enhancement of the nanostructures. The distance between the nanorings in a dimer can be varied by controlling the length of the Ni segments (Figure 3b).

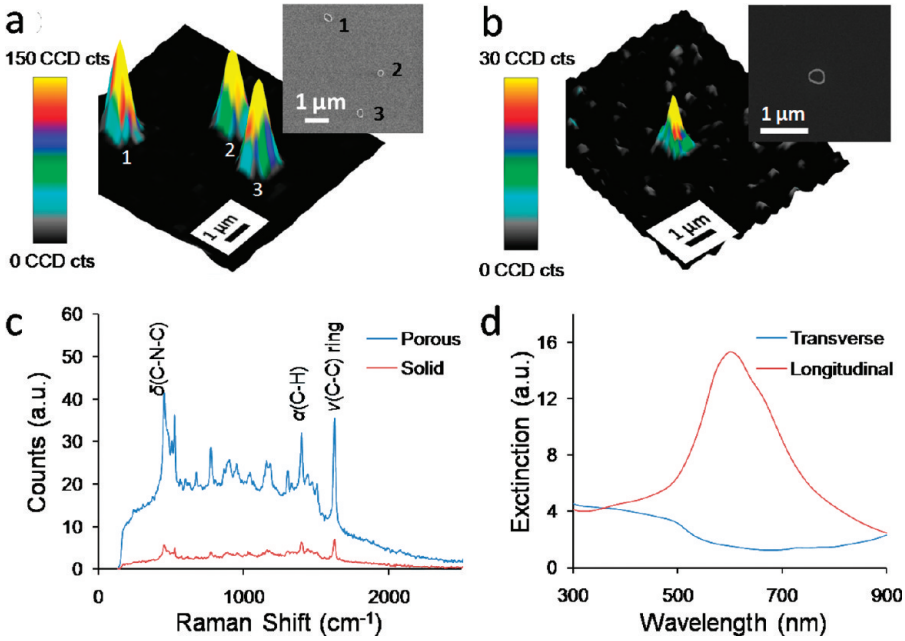

Figure 2. 3D scanning Raman microscopy images of (a) porous nanorings and (b) a solid nanoring. The dimensions of both nanorings are as follows: inner diameter, ~360 nm; wall thickness, ~35 nm; and length, ~100 nm. Insets show SEM images of the corresponding nanorings. (c) The average Raman spectrum of MB from both porous nanorings and solid nanorings. (d) Calculated extinction spectra of nanoring for longitudinal and transverse polarization of light based on DDA calculations. The dimensions of the nanorings are as follows: inner diameter, 360 nm; wall thickness, 36 nm; and length, 100 nm.

With this method, we have fabricated a series of nanoring dimers. Moreover, we have compared them with Au nanodisk dimers[17] (Figure 4a inset). The Au nanodisks have an average diameter of 360 ± 24 nm and length of 120 ± 17 nm; with a plasmon resonance that is in resonance with the 633 nm incident laser (Figure 4c).[17] The nanoring dimers also have similar dimensions (357 ± 26 nm inner diameter and 35 ± 10 nm wall thickness). The length of each nanoring was deliberately varied from 77 to 210 nm to find an optimized length with respect to SERS. The gap in the nanoring dimers and nanodisk dimers are ~100 nm wide; which is optimum to have significant coupling, while also large enough to keep the rings from coming in physical contact (the gold grows nonuniformly on the surface of the rings creating

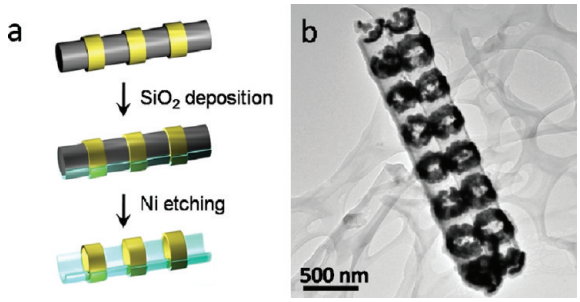

Figure 3. (a) Scheme illustrating the fabrication of nanoring arrays by SiO_2 deposition to one side of GRR-modified-nanorods, followed by wet chemical etching of Ni. (b) Tilted-view TEM image of nanoring arrays on a SiO_2 backing layer. The array consists of six nanorings with an average length of 120 nm and a 300 nm separation between nanorings. Note that there are some particles at both ends of the arrays that grew during the GRR.

a nonideal corrugated surface, Figure 1c). The dimers were separated by 1 μm to prevent any plasmonic interaction. These arrays, like their SiO_2-backing free analogues above, were functionalized with MB and characterized by Raman microscopy.

A Raman map of a structure with both ring and disk dimers shows that the nanoring dimers with an average ring length of 130 ± 13 nm give the highest Raman intensity (Figure 4a). This large field enhancement is due to the overlap of the plasmon resonance of this structure with the laser wavelength, as verified by DDA calculations (Figure 4b). Indeed, the calculated extinction spectra of nanoring dimers as a function of ring length show that the structures with a 120 nm ring length are optimized with respect to spectral overlap with the incident laser. The calculated field profile for this case (Supporting Information, Figure S3) shows a strong dipole resonance, with highest enhancements on the inner wall of the ring.

For comparison purposes, we have plotted the Raman intensity ratio of the nanoring dimers and the Au nanodisk dimers as a function of nanoring length (Figure 4c). Each experimental point on the graph was taken from an average of at least five samples. The calculated intensity ratio is also plotted in the same graph. Both experiment and calculation are in good agreement, showing that a nanoring dimer with a length between 100 and 160 nm gives an intensity ratio larger than 1. This also means that in this region of the graph, the enhancing properties of the rings have been optimized with respect to the disks.

There are two factors that differentiate these nanorings from Au nanodisks: composition and geometry. The nanorings are bimetallic while the nanodisks are pure gold. To differentiate these factors, we calculated the average SERS enhancement factor

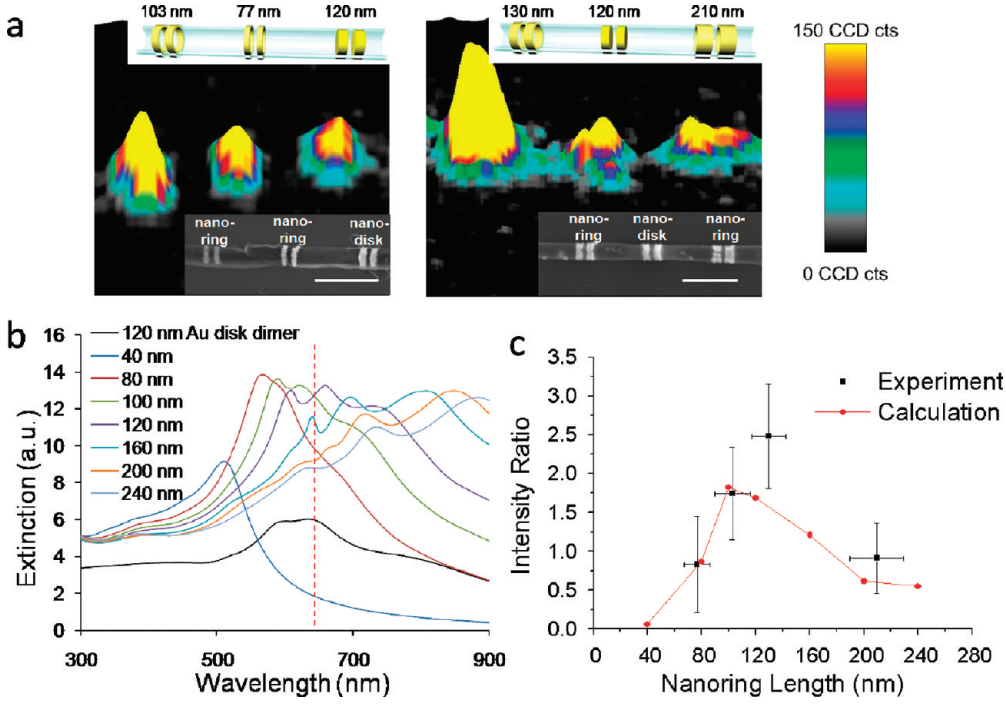

Figure 4. (a) 3D scanning Raman microscope images of nanoring dimers and nanodisk dimers. The dimensions of the nanorings are as follows: inner diameter, ~360 nm; wall thickness, ~35 nm; and length, varies as denoted in the insets (*i.e.*, 103, 77, 130, and 210 nm, respectively). The dimensions of the nanodisks are as follows: diameter, ~360 nm; length, ~120 nm. All gaps sizes are ~100 nm. Insets show SEM images of the arrays (scale bar: 1 μm). (b) Theoretical extinction spectra of Au/Ag (1:1) alloy nanoring dimers with different lengths and of 120 nm Au nanodisk dimer calculated by the DDA method. Laser excitation wavelength at 633 nm is shown for clarity. (c) The experimental and calculated Raman intensity ratio (Au/Ag nanoring dimers divided by 120 nm Au nanodisk dimer) *versus* nanoring length.

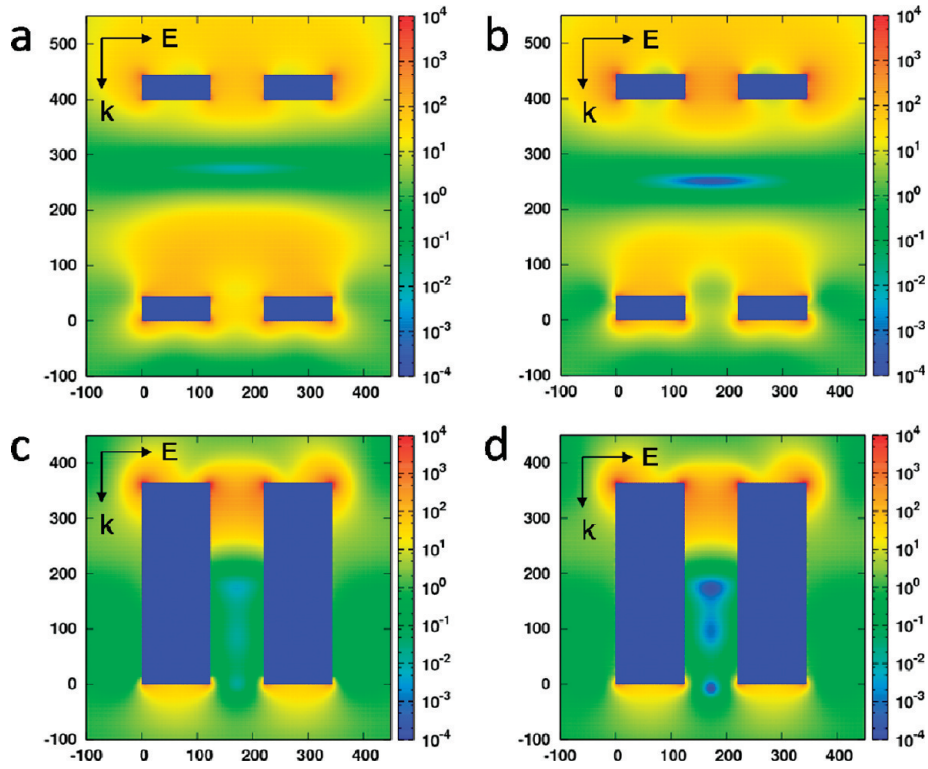

Figure 5. Contours of SERS enhancement factors for (a) Au nanoring dimer, (b) Au/Ag (1:1) nanoring dimer, (c) Au nanodisk dimer, and (d) Au/Ag (1:1) nanodisk dimer. The dimensions of the nanorings are as follows: inner diameter, 360 nm; wall thickness, 40 nm; and length, 120 nm. The dimensions of the nanodisks are as follows: diameter, 360 nm; length, 120 nm. The *x* and *y* axes are distances in nm. Note that the coordinates of the plot cut through the center of the nanoring and nanodisk such that the ring forms two rectangles, 40 nm × 120 nm while the disk forms one rectangle, 360 nm × 120 nm. Laser excitation is at 633 nm.

for 633 nm irradiation of four different systems using the DDA method (Figure 5): Au ring dimer, alloy (Ag/Au = 1/1) ring dimer, Au disk dimer, and alloy (Ag/Au = 1/1) disk dimer. The dimensions of the rings and disks mimic the experimental value (for rings, inner diameter = 360 nm, length = 120 nm, wall thickness = 40 nm; for disks, diameter = 360 nm, length = 120 nm). Note that the DDA calculations determine the fields half a grid spacing away from the true surface of the particles. Since the grid spacing is 4 nm, the calculated fields will be well below the actual surface fields. This is not important for the present application where only the change in enhancement in going from one structure to another is important; however, the absolute enhancement factors are likely to be 1−2 orders of magnitude higher than we have calculated.

The SERS enhancement factors for structures of different composition are similar, indicating that the Au/Ag alloy and gold dielectric properties are close (Figure 5). In contrast, the enhancement factors for different structures are drastically different. The electric fields are strongly enhanced over the entire ring surface, while only small portions and selected areas of the disk surface show strong enhancements. As a result, the average enhancement factor (estimated by averaging over the accessible surfaces of the nanostructures) for the Au ring dimer (EF = 314) and the alloy ring dimer (345) are about twice that for the Au disk dimer (171) and alloy disk dimer (149). On the basis of these studies, we conclude that the geometry of nanostructures plays a much more significant role compared to the composition in our system. Note that if the enhancements were averaged only over the available surfaces (in experiment, some of the surfaces are covered by SiO_2), the structures show similar enhancement factors.

In conclusion, we have fabricated bimetallic nanorings and nanoring arrays by a new method based on OWL and a GRR. There are several attributes to this method. First, we can easily tune the length of the nanorings by altering the length of the Ag segments in the precursor, thus providing diverse aspect ratios. Second, the diameter of the nanorings, in principle, can also be tuned by using different pore sizes of the AAO template.[40] Third, one can make these structures in relatively high yield with moderate throughput, making them potentially useful as spectroscopic labels. Finally, these features enable us to tune the LSPR peak wavelengths of the nanorings over a wide range, allowing for both optimization of the nanostructures and fundamental understanding of the origins of their spectroscopic properties.

METHODS

Striped Ag—Ni Nanorod Structures Made by Electrochemical Deposition. To make Ag—Ni nanorods, 200 nm of Ag was first evaporated onto one side of an AAO membrane (Whatman Anodisc, pore size 0.02 μm—only at the end of the pore, the actual pore size is ~360 nm), which served as a working electrode for electrochemical deposition. This template was then placed in an electrochemical cell with Ag/AgCl as a reference electrode and Pt as a counter-electrode. Ag was electrodeposited first (at −950 mV, 6 C) from the commercially available solution (Technic Inc. 1025 RTU @ 4.5 troy/gallon) to let Ag grow into the pores. Afterward, the cell was washed and refilled with Ni solution (Technic, Inc., nickel sulfamate RTU). Subsequent alternating depositions of Ni (at −1000 mV) and Ag (−1100 mV) were done to get striped nanorods. The corresponding deposition rates were approximately 9 nm s^{-1} for both Ag and Ni, which were considered as fast depositions to generate a relatively smooth end-surface. The total charge during deposition controls the segment lengths (Supporting Information, Figure S1). To release the nanorods from the AAO template, the backing layer (evaporated and electrodeposited Ag) was chemically etched by methanol/H_2O_2/NH_4OH (4:1:1 v/v) for 20 min, and then the process continued with AAO template dissolution by 3 M NaOH for 20 min. The released rods were then rinsed with deionized water three times and kept in 2 mL of H_2O.

Galvanic Replacement Reaction (GRR). GRR was performed by dispersing 1 mL of the striped nanorods in a 10 mL boiling aqueous solution of $HAuCl_4$ (concentration varies depending on the size of Ag segments, *i.e.*, 30 μM for 0.9 C Ag deposition) for 10 min. Ag was consumed during the reaction as evidenced by TEM (Supporting Information, Figure S2a), where the nanoring segments appear more transparent compared to the Ni segments. The solution was later centrifuged and rinsed twice with water to obtain bimetallic nanorings at the positions occupied by the Ag segments. To release the nanorings, Ni segments were completely etched in 35—38% HCl for 3 h.

Nanoring Arrays Fabrication by OWL. The modified nanorods (nanorods after GRR) were dispersed in H_2O. The suspension was dropped on precleaned glass slides and left overnight to dry. The glass slides were put in the PECVD chamber (PLASMALAB μP, Plasma Technology, Inc., Torrance, CA), which was pumped to high vacuum, and the glass slides were heated to 240 °C. Then, N_2O and SiH_4/N_2 (10%/90%) gases were introduced into the chamber at flow rates of 400 and 40 sccm, respectively. The pressure was kept at 200 mTorr by adjusting the throttle, and the RF power was set at 18 W. The corresponding deposition rate was 10 nm/min. Deposition was run for 5 min to get a silica layer with thickness of 50 nm. The silica-coated nanorods were released from the glass slides by sonication in ethanol for 8 s. The final step of this process involves wet chemical etching of Ni segments by HCl (36.5—38.0%) for at least 3 h.

Acknowledgment. C.A.M. acknowledges a NSSEFF Fellowship from DoD and grant support from the NSF NSEC (EEC-0647560), the DOE Office (Award No. DE-SC0000989) for support via the NU Non-equilibrium Energy Research Center, and AFOSR. C.L. is grateful for a STRAT Fellowship from EDB in Singapore. S.L. and G.C.S. were supported by the NSEC grant. SEM and TEM images were taken on a Hitachi S-4800-II cFEG SEM and a Hitachi H-8100 TEM, respectively, courtesy of Northwestern University NUANCE Center.

Supporting Information Available: SEM and TEM images, EDX spectrum, plot of segment length in nanorods *vs* charge passed through during electrochemical deposition, and SERS enhancement factor contour plot for solid Au/Ag (1:1) nanorings. This material is available free of charge *via* the Internet at http://pubs.acs.org.

REFERENCES AND NOTES

1. Barnes, W. L.; Dereux, A.; Ebbesen, T. W. Surface Plasmon Subwavelength Optics. *Nature* **2003**, *424*, 824–830.
2. Mirkin, C. A.; Letsinger, R. L.; Mucic, R. C.; Storhoff, J. J. A DNA-Based Method for Rationally Assembling Nanoparticles into Macroscopic Materials. *Nature* **1996**, *382*, 607–609.
3. Wang, J. J.; Saito, Y.; Batchelder, D. N.; Kirkham, J.; Robinson, C.; Smith, D. A. Controllable Method for the Preparation of Metalized Probes for Efficient Scanning Near-Field Optical Raman Microscopy. *Appl. Phys. Lett.* **2005**, *86*, 263111.
4. Service, R. F. Solar Energy: Can the Upstarts Top Silicon. *Science* **2008**, *319*, 718–720.
5. Xue, C.; Mirkin, C. A. pH-Switchable Silver Nanoprism Growth Pathways. *Angew. Chem., Int. Ed.* **2007**, *46*, 2036–2038.
6. Zhang, J.; Li, S.; Wu, J.; Schatz, G. C.; Mirkin, C. A. Plasmon-Mediated Synthesis of Silver Triangular Bipyramids. *Angew. Chem., Int. Ed.* **2009**, *48*, 7787–7791.
7. Jana, N. R.; Gearheart, L.; Murphy, C. J. Wet Chemical Synthesis of High Aspect Ratio Cylindrical Gold Nanorods. *J. Phys. Chem. B* **2001**, *105*, 4065–4067.
8. Wang, H.; Brandl, D. W.; Nordlander, P.; Halas, N. J. Plasmonic Nanostructures: Artificial Molecules. *Acc. Chem. Res.* **2007**, *40*, 53–62.
9. Lu, X.; Au, L.; McLellan, J.; Li, Z.-Y.; Marquez, M.; Xia, Y. Fabrication of Cubic Nanocages and Nanoframes by Dealloying Au/Ag Alloy Nanoboxes with an Aqueous Etchant Based on $Fe(NO_3)_3$ or NH_4OH. *Nano Lett.* **2007**, *7*, 1764–1769.
10. Sönnichsen, C.; Franzl, T.; Wilk, T.; von Plessen, G.; Feldmann, J.; Wilson, O.; Mulvaney, P. Drastic Reduction of Plasmon Damping in Gold Nanorods. *Phys. Rev. Lett.* **2002**, *88*, 077402.
11. Aizpurua, J.; Hanarp, P.; Sutherland, D. S.; Käll, M.; Bryant, G. W.; García de Abajo, F. J. Optical Properties of Gold Nanorings. *Phys. Rev. Lett.* **2003**, *90*, 057401.
12. McLellan, J. M.; Geissler, M.; Xia, Y. Edge Spreading Lithography and Its Application to the Fabrication of Mesoscopic Gold and Silver Rings. *J. Am. Chem. Soc.* **2004**, *126*, 10830–10831.
13. Larsson, E. M.; Alegret, J.; Kall, M.; Sutherland, D. S. Sensing Characteristics of NIR Localized Surface Plasmon Resonances in Gold Nanorings for Application as Ultrasensitive Biosensors. *Nano Lett.* **2007**, *7*, 1256–1263.
14. Yang, S. M.; Jang, S. G.; Choi, D. G.; Kim, S.; Yu, H. K. Nanomachining by Colloidal Lithography. *Small* **2006**, *2*, 458–475.
15. Yu, X.; Zhang, H.; Oliverio, J. K.; Braun, P. V. Template-Assisted Three-Dimensional Nanolithography *via* Geometrically Irreversible Processing. *Nano Lett.* **2009**, *9*, 4424–4427.
16. Banaee, M. G.; Crozier, K. B. Gold Nanorings as Substrates for Surface-Enhanced Raman Scattering. *Opt. Lett.* **2010**, *35*, 760–762.
17. Zhao, S.; Roberge, H.; Yelon, A.; Veres, T. New Application of AAO Template: A Mold for Nanoring and Nanocone Arrays. *J. Am. Chem. Soc.* **2006**, *128*, 12352–12353.
18. Zinchenko, A. A.; Yoshikawa, K.; Baigl, D. DNA-Templated Silver Nanorings. *Adv. Mater.* **2005**, *17*, 2820–2823.
19. Behrens, S.; Habicht, W.; Wagner, K.; Unger, E. Assembly of Nanoparticle Ring Structures Based on Protein Templates. *Adv. Mater.* **2006**, *18*, 284–289.
20. Qin, L.; Zou, S.; Xue, C.; Atkinson, A.; Schatz, G. C.; Mirkin, C. A. Designing, Fabricating, and Imaging Raman Hot Spots. *Proc. Natl. Acad. Sci. U.S.A.* **2006**, *103*, 13300–13303.
21. Qin, L.; Banholzer, M. J.; Millstone, J. E.; Mirkin, C. A. Nanodisk Codes. *Nano Lett.* **2007**, *7*, 3849–3853.
22. Qin, L.; Park, S.; Huang, L.; Mirkin, C. A. On-Wire Lithography. *Science* **2005**, *309*, 113–115.
23. Chen, X.; Jeon, Y.-M.; Jang, J.-W.; Qin, L.; Huo, F.; Wei, W.; Mirkin, C. A. On-Wire Lithography-Generated Molecule-Based Transport Junctions: A New Testbed for Molecular Electronics. *J. Am. Chem. Soc.* **2008**, *130*, 8166–8168.
24. Chen, X.; Yeganeh, S.; Qin, L.; Li, S.; Xue, C.; Braunschweig, A. B.; Schatz, G. C.; Ratner, M. A.; Mirkin, C. A. Chemical Fabrication of Heterometallic Nanogaps for Molecular Transport Junctions. *Nano Lett.* **2009**, *9*, 3974–3979.

25. Chen, X.; Braunschweig, A. B.; Wiester, M.; Yeganeh, S.; Ratner, M. A.; Mirkin, C. A. Spectroscopic Tracking of Molecular Transport Junctions Generated by Using Click Chemistry. *Angew. Chem., Int. Ed.* **2009**, *48*, 5178–5181.
26. Zheng, G.; Qin, L.; Mirkin, C. A. Spectroscopically Enhancing Electrical Nanotraps. *Angew. Chem., Int. Ed.* **2008**, *47*, 1938–1941.
27. Qin, L.; Banholzer, M. J.; Xu, X.; Huang, L.; Mirkin, C. A. Rational Design and Synthesis of Catalytically Driven Nanorotors. *J. Am. Chem. Soc.* **2007**, *129*, 14870–14871.
28. Wei, W.; Li, S.; Qin, L.; Xue, C.; Millstone, J. E.; Xu, X.; Schatz, G. C.; Mirkin, C. A. Surface Plasmon-Mediated Energy Transfer in Heterogap Au−Ag Nanowires. *Nano Lett.* **2008**, *8*, 3446–3449.
29. Metraux, G. S.; Cao, Y. C.; Jin, R.; Mirkin, C. A. Triangular Nanoframes Made of Gold and Silver. *Nano Lett.* **2003**, *3*, 519–522.
30. Zhang, H.; Jin, R.; Mirkin, C. A. Synthesis of Open-Ended, Cylindrical Au−Ag Alloy Nanostructures on a Si/SiO_x Surface. *Nano Lett.* **2004**, *4*, 1493–1495.
31. Martin, B. R.; Dermody, D. J.; Reiss, B. D.; Fang, M.; Lyon, L. A.; Natan, M. J.; Mallouk, T. E. Orthogonal Self-Assembly on Colloidal Gold−Platinum Nanorods. *Adv. Mater.* **1999**, *11*, 1021–1025.
32. Erlebacher, J.; Aziz, M. J.; Karma, A.; Dimitrov, N.; Sieradzki, K. Evolution of Nanoporosity in Dealloying. *Nature* **2001**, *410*, 450–453.
33. Hutchinson, K.; Hester, R. E. Raman Spectroscopic Studies of a Thionine-Modified Electrode. *J. Chem. Soc., Faraday Trans. 1* **1984**, *80*, 2053–2071.
34. Draine, B. T.; Flatau, P. J. Discrete-Dipole Approximation for Periodic Targets: Theory and Tests. *J. Opt. Soc. Am. A* **2008**, *25*, 2693–2703.
35. Zhao, J.; Pinchuk, A. O.; McMahon, J. M.; Li, S.; Ausman, L. K.; Atkinson, A. L.; Schatz, G. C. Methods for Describing the Electromagnetic Properties of Silver and Gold Nanoparticles. *Acc. Chem. Res.* **2008**, *41*, 1710–1720.
36. Li, S.; Pedano, M. L.; Chang, S.-H.; Mirkin, C. A.; Schatz, G. C. Gap Structure Effects on Surface-Enhanced Raman Scattering Intensities for Gold-Gapped Rods. *Nano Lett.* **2010**, *10*, 1722–1727.
37. Draine, B. T.; Flatau, P. J. User Guide for the Discrete Dipole Approximation Code DDSCAT 7.0. http://arxiv.org/abs/0809.0337v4, 2008.
38. Johnson, P. B.; Christy, R. W. Optical Constants of the Noble Metals. *Phys. Rev. B* **1972**, *6*, 4370.
39. Lynch, D. W.; Hunter, W. R. Comments on the Optical Constants of Metals and an Introduction to the Data for Several Metals. In *Handbook of Optical Constants of Solids*; Palik, E. D., Ed.; Academic Press: New York, 1985; p 350.
40. Zhang, J.; Kielbasa, J. E.; Carroll, D. L. Controllable Fabrication of Porous Alumina Templates for Nanostructures Synthesis. *Mater. Chem. Phys.* **2010**, *122*, 295–300.